Chaos in conservative discrete-time systems subjected to parameter drift

Cite as: Chaos **31**, 033142 (2021); https://doi.org/10.1063/5.0031660
Submitted: 02 October 2020 . Accepted: 02 March 2021 . Published Online: 18 March 2021

Dániel Jánosi, and Tamás Tél

Chaos in conservative discrete-time systems subjected to parameter drift

Cite as: Chaos **31**, 033142 (2021); doi: 10.1063/5.0031660
Submitted: 2 October 2020 · Accepted: 2 March 2021 ·
Published Online: 18 March 2021

Dániel Jánosi[1,a] and Tamás Tél[1,2,b]

AFFILIATIONS

[1] Institute for Theoretical Physics, Eötvös Loránd University, Pázmány Péter Sétány 1/A, H-1117 Budapest, Hungary
[2] MTA-ELTE Theoretical Physics Research Group, Pázmány Péter Sétány 1/A, H-1117 Budapest, Hungary

[a] **Author to whom correspondence should be addressed:** daniel.janosi@ttk.elte.hu
[b] **Electronic mail:** tel@general.elte.hu

ABSTRACT

Based on the example of a paradigmatic area preserving low-dimensional mapping subjected to different scenarios of parameter drifts, we illustrate that the dynamics can best be understood by following ensembles of initial conditions corresponding to the tori of the initial system. When such ensembles are followed, snapshot tori are obtained, which change their location and shape. Within a time-dependent snapshot chaotic sea, we demonstrate the existence of snapshot stable and unstable foliations. Two easily visualizable conditions for torus breakup are found: one in relation to a discontinuity of the map and the other to a specific snapshot stable manifold, indicating that points of the torus are going to become subjected to strong stretching. In a more general setup, the latter can be formulated in terms of the so-called stable pseudo-foliation, which is shown to be able to extend beyond the instantaneous chaotic sea. The average distance of nearby point pairs initiated on an original torus crosses over into an exponential growth when the snapshot torus breaks up according to the second condition. As a consequence of the strongly non-monotonous change of phase portraits in maps, the exponential regime is found to split up into shorter periods characterized by different finite-time Lyapunov exponents. In scenarios with plateau ending, the divided phase space of the plateau might lead to the Lyapunov exponent averaged over the ensemble of a torus being much smaller than that of the stationary map of the plateau.

In an earlier paper,[1] we explored some properties of low-dimensional Hamiltonian systems subjected to parameter drifts, based on time-continuous descriptions. Here, we are extending the investigation to discrete-time dynamical systems described by mappings. In this class, new features can show up due to discontinuities arising in the dynamics, which can also be a consequence of physical reasons. The phase portrait of stationary maps can dramatically change with parameters, and even fully chaotic phase spaces might exist without any Kolmogorov–Arnold–Moser (KAM) tori. These all can have consequences for the dynamics observable in the presence of parameter drifts. Some features, e.g., different forms of foliations, can be studied in more detail since numerical investigations are much faster for maps than for differential equations.

I. INTRODUCTION

Area preserving or Hamiltonian systems subjected to parameter drifts are of interest in a number of instances:

- adiabatic invariants with quasi-statically slow drifts,[2–5]
- Lagrangian coherent structures in flows of arbitrary time dependence (see, e.g., Refs. 6–10),
- plasma physics, where via manipulating the time-dependent magnetic structure at the plasma edge, the shape of the chaotic sea can be influenced,[11–14]
- ultracold atoms, where a control parameter can be swept and experiments are also possible,[15,16]
- atomic scattering off a vibrating surface,[17]
- chemical reactions across anharmonically driven barriers.[18,19]

The literature is, however, still sparse compared with that on dissipative systems, where a clear analogy can be seen with climate change. In systems of arbitrary time dependence, the concept of the snapshot attractor was introduced.[20–27] Here, long-term investigation of single trajectories is inappropriate and a consistent picture can only be obtained by launching trajectories from a large number of different initial conditions, i.e., following an initially extended ensemble in the phase space. This way, the snapshot attractor is the image of the ensemble in a given time instant, as illustrated in

Refs. 20, 28, and 29. This approach has successfully been applied to large-scale climate models (for recent applications, see, e.g., Refs. 30–33), turbulence-related experiments,[34] and most recently to epidemics.[35]

By taking over the observation that individual time series are not representative, we have shown in Ref. 1 that ensembles should be used in Hamiltonian cases as well, although these have to be selected with care. One candidate providing good insight is based on ensembles starting on KAM tori of the initial phase space. As time goes on, these ensembles evolve, and as long as they can be considered to be closed curves, we have proposed to call them *snapshot tori*. Being exposed to parameter drifts, at some point, most of the tori start to break up; i.e., they cease to appear as closed curves by experiencing intense stretching.

A more careful investigation has revealed[1] that chaotic seas in such systems are also time-dependent. Inside them, orbits are expected to exist with locally hyperbolic nearby dynamics, a property valid while the orbit is changing in time. Such points we called *snapshot hyperbolic points* (SHPs). Their stable and unstable manifolds were found to intersect in several points at any time: a snapshot horseshoe or a snapshot chaotic saddle[36] is created.

In this paper, we illustrate analogous features of conservative systems described by mappings. Our illustrative example, the double wedge,[37–39] is chosen with the intention of also illustrating a possible feature of maps, a discontinuity arising in the dynamics because of physical reasons. Apart from this feature, the map is paradigmatic and exhibits generic properties, e.g., a divided phase space in a broad range of parameters. After introducing the map, reviewing its most important stationary properties and defining the parameter drift in Sec. II, we demonstrate that in a map with a structural discontinuity in the dynamics, a snapshot torus breaks up, ceasing to be a continuous curve, when it crosses the discontinuity line in the phase space (Sec. III). Among others, we also find the surprising property that the snapshot torus might remain continuous and exist even in a parameter range where the stationary problem is fully chaotic for certain scenarios at least. Another condition also holds, which occurs when a torus collides with a stable manifold of a hyperbolic point belonging to a later time instant. An analog question was discussed in Ref. 1 in the analytic knowledge of the location of a snapshot hyperbolic point. Such a case is, however, extremely rare, and such a point cannot be identified in our map system either. We point out how one can proceed in such a general case and show that any element of a hyperbolic cycle of the stationary system can be a good candidate for playing the role of the aforementioned hyperbolic point. As discussed in Sec. IV, this is the dynamical condition being the precursor of the torus becoming subjected to intense stretching. This condition, as well as the properties discussed in Secs. V–VII, holds for two-dimensional maps without any discontinuity in their dynamics as well. This is illustrated with the example of the standard map subjected to an increasing nonlinearity parameter in the supplementary material.

We show that the dynamical character of an ensemble initiated on a torus can be monitored in discrete-time systems, too, by a quantity called *ensemble-averaged pairwise distance* (Sec. V). For most of the tori, there exists a crossover time after which the ensemble starts exhibiting chaos-like dynamics. The slope of this quantity can be considered an instantaneous Lyapunov exponent. The crossover time depends on both the torus in question and the drift scenario to which the system is subjected. The strongly non-monotonous parameter dependence of the phase space pattern in the stationary problem might lead to the alteration of stronger and weaker dynamical instability (larger and smaller instantaneous Lyapunov exponents) along a single scenario in the presence of parameter drifts (Sec. V). In Sec. VI, non-monotonous drifts are considered. When the scenario ends in a plateau, tori seem to survive during long periods in chaotic seas belonging to the plateau value. The Lyapunov exponent averaged over the ensemble of a torus can be much smaller than that of the stationary map of the plateau. In scenarios with full return, pronounced hysteresis occurs. Investigating the structure of snapshot chaotic seas (Sec. VII), we demonstrate that the stable and unstable foliations remain inside of them, but a special version, the so-called stable pseudo-foliation, is shown to be able to extend beyond the instantaneous chaotic sea. A general formulation of the dynamical condition for torus breakup can also be given in terms of this foliation. Auxiliary information is given in the supplementary material.

II. THE DOUBLE WEDGE

A. The fixed angle case

As a paradigmatic system, we choose the double wedge.[37–39] Take two slopes facing each other, which form the same angle α with the horizontal. On one of these slopes, we drop a ball that starts to bounce perfectly flexibly. The motion of the ball is naturally followed in discrete time by using the components of the velocity vector parallel (u) and perpendicular (w) to the slope, taken at the moments when the ball collides with the slope. Frictional forces are negligible, and the ball is considered point-like. Then, the relationship between the velocity components u_n, w_n of the nth collision and the components u_{n+1}, w_{n+1} characteristic of the next collision can be derived from the equations of oblique projection.[37–39]

The component w perpendicular to the slope is always taken at the moment after the collision. To make the presentation clearer, it is worth using dimensionless velocities and the square of the w component instead. With the notation $z = w^2$, the mapping is[38,39]

$$\begin{aligned} u_{n+1} &= u_n - 2\sqrt{z_n}\,\mathrm{tg}\,\alpha, \\ z_{n+1} &= z_n \end{aligned} \tag{1}$$

if $u_{n+1}^2 + z_{n+1} \le 1$; otherwise the mapping is described by

$$\begin{aligned} u_{n+1} &= -u_n + \sqrt{z_n}\,\mathrm{tg}\,\alpha - \sqrt{z_{n+1}}\,\mathrm{tg}\,\alpha, \\ z_{n+1} &= -z_n\left(1 + \frac{1}{2}\sin 4\alpha\,\mathrm{tg}\,\alpha\right) - u_n^2\frac{1}{2}\sin 4\alpha\,\mathrm{ctg}\,\alpha \\ &\quad + u_n\sqrt{z_n}\sin 4\alpha + 2\cos^2\alpha. \end{aligned} \tag{2}$$

Switching between the two formulas occurs when the ball jumps on the opposite slope.[37–39] This can be formulated by defining a line in the phase space,

$$u(z) = 2\sqrt{z}\,\mathrm{tg}\,\alpha - \sqrt{1-z}, \tag{3}$$

and realizing that (1) and (2) hold when $u_n \le u(z_n)$ and $u_n \ge u(z_n)$, respectively. Line (3) expresses the condition where a structural discontinuity occurs in the dynamics, and we call it, therefore, the line of discontinuity.

Plotting the perpendicular z as a function of the parallel u yields a Poincaré map of the phase space. Its extension is restricted to a specific range; this is the parabola $z = 1 - u^2$ and the area below it [see Fig. 1(a)].

The phase portrait is that of a mixed phase space for angles $45^\circ < \alpha < 90^\circ$. The particular pattern, however, depends on the angle in a strongly non-monotonous way; see Figs. 1(b)–1(f). If α is less than 45°, no macroscopic sized tori are found numerically, and all initial conditions yield chaotic motion, as stated in Refs. 37–39, and illustrated, e.g., in Fig. 1(f). The case of $\alpha = 45^\circ$ corresponds to a special chaos-free phase space in which only quasiperiodic motions belonging to periodic or constant z values can occur [Fig. 1(e)].

For the 70° and 55° wedges, since all tori are above the line of discontinuity (green curve), quasiperiodic motions only occur when the ball bounces on opposite slopes. In the 50° case, because there are tori under the green curve, the ball can bounce both on the same and opposite slopes within a period of approximate return of three bounces.

For bounces between the opposite slopes, there exists a single fixed point with coordinates $u^* = 0$ and

$$z^* = \frac{1}{2 - \cos(2\alpha)}. \tag{4}$$

This is the center point (marked with an orange dot) of the innermost tori in the panels, which corresponds to a movement in the real space where the ball bounces between two exactly opposite points, always arriving perpendicular to the slope. This periodic motion is always unstable below 45° (the fixed point is part of the chaotic sea), while above 45°, the fixed point is elliptic.

There exists of course an infinity of higher order cycles in the system; see Ref. 38 for example. Here, we give the coordinates of a three-cycle with two points above the discontinuity line, like the one found in Fig. 1(d), as a function of α. The leftmost element is located at

$$u_0^* = -\frac{\sin\alpha}{\Gamma} \quad z_0^* = \frac{\cos^2\alpha}{\Gamma^2}, \tag{5}$$

where $\Gamma^2 = \sin 4\alpha \ \mathrm{tg}\ \alpha + 5/2$, while the uppermost point is at $u_1^* = 0$, $z_1^* = 4z_0^*$ and the rightmost one at $u_2^* = -u_0^*$, $z_2^* = z_0^*$. This cycle only exists between angles 30° and 60°.

B. Wedge with a changing angle

When turning to cases when the common angle of the wedges changes with time, there are different options to make the mapping non-autonomous. We take the simplest possible extension of the model by allowing the angle to be time-dependent in the sense that the fixed α value is replaced by a collision-number-dependent α_n; in other words,

$$\alpha \to \alpha_n \tag{6}$$

is taken in (1) and (2) (see Fig. 2). The flight after the nth bounce starts from a wedge of angle α_n, and the formulas determine the new velocity coordinates for when the particle arrives at the slope

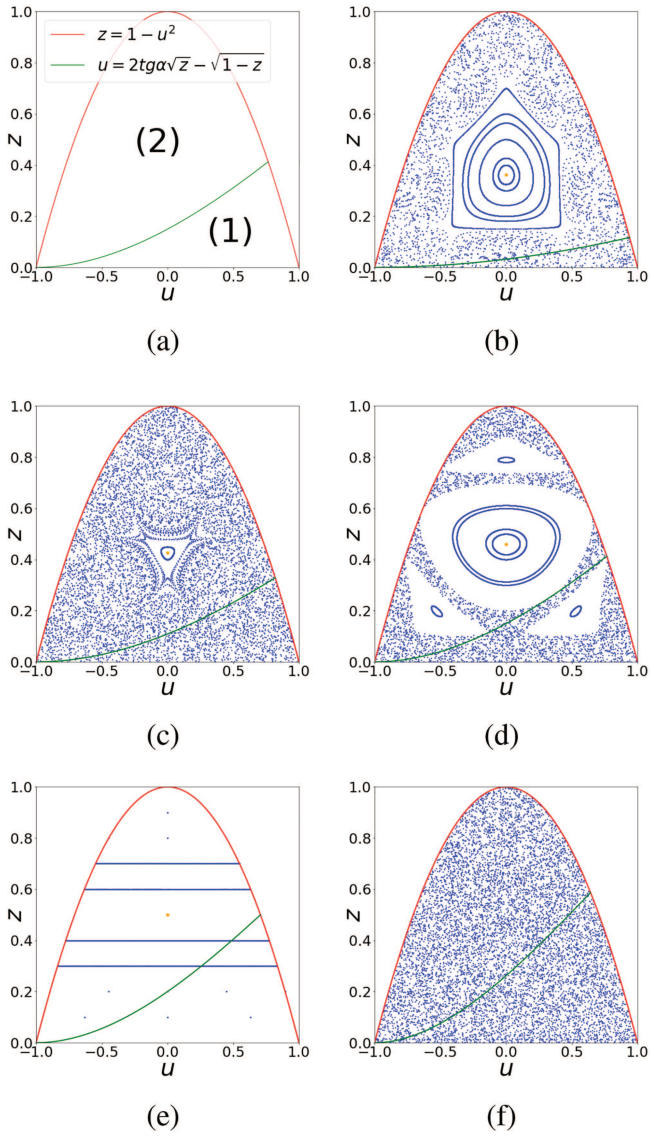

FIG. 1. (a) The green discontinuity line (3) and how it divides the phase space between mappings (1) and (2), with $\alpha = 50^\circ$, the red parabola being the limit of validity of the dynamics. (b)–(f) Phase portraits for angles $\alpha = 70^\circ, 55^\circ, 50^\circ, 45^\circ$, and 40°. In each case, trajectories were started from nine initial conditions so that u_0 is always 0 and $z_0 = 0.1, 0.2, \ldots, 0.9$, and each starting point was followed up to 1000 iterations. Note that the phase portraits are not monotonously dependent on the angle.

for the $n+1$th collision. *After this*, we change the angle from α_n to some α_{n+1} and let the particles fly afterward according to (1) and (2) applied with α_{n+1}.

As a consequence, in the nth iterate, the discontinuity condition (3) is replaced in the phase space (u, z) by

$$u(z) = 2\sqrt{z}\,\mathrm{tg}\,\alpha_n - \sqrt{1-z}. \tag{7}$$

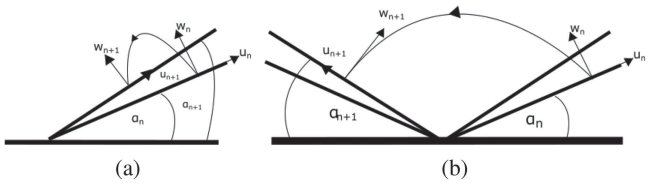

FIG. 2. Schematic picture of the bouncing ball dynamics on the wedge with a changing angle. The motions described by mappings (1) and (2) are attributed to cases (a) and (b), respectively, with $z = w^2$ taken in the formulas.

A more realistic extension of the model is described in Sec. S1 of the supplementary material where the angle is changed *during* the flight; i.e., after starting from a slope of angle α_n, the next bounce occurs on a slope of angle α_{n+1}. Since the numerical properties of the two models hardly differ, as also illustrated by Fig. S1 of the supplementary material, we shall study the simple approach corresponding to (6) throughout the paper. The stationary mappings (1) and (2) follow from the derivation given in Sec. S1 of the supplementary material as a special case.

A *scenario* is a sequence of the angles α_n, starting from some α_0. We shall typically fix the final angle α_f, too, and apply a fixed, signed increment $\Delta\alpha$ in N steps, the length of the scenario. This way, the increment can be written as $\Delta\alpha = (\alpha_f - \alpha_0)/N$. A scenario like this will be denoted by the triplet $[\alpha_0, \alpha_f, N]$.

We shall also need the inverse map. For a fixed angle, it is of the same form as (1) and (2), just all u variables are to be replaced by $-u$. In this new form, n of course means the index of the initial bounce in the inverse, i.e., the last bounce in the direct dynamics. The inverse of the non-autonomous map turns out to keep this property. Since, however, the new angle value is set in the direct dynamics after the flight is over, in the inverse, the dynamics should be taken with the angle changed earlier, and accordingly, when applying the inverse map in the nth iterate, the discontinuity line is given by (7) with α_n replaced by α_{n+1} and u by $-u$.

III. SNAPSHOT TORI AND IMPLICATIONS

A. Evolution of tori in different scenarios

In Ref. 1, it was shown that Hamiltonian systems with parameter drift are best described with special initial ensembles corresponding to the tori of the stationary system, and the evolution of these ensembles is worth following under the parameter drift. The shape of these ensembles is called snapshot tori at every instant before they break up. We apply the same method to the investigated discrete-time systems.

Figure 3 shows a typical scenario, with a few snapshot tori followed. One sees that the tori become more and more deformed as time goes on. In Fig. 3(c), a new feature appears: the tori become cut into several pieces. This is a mechanism characteristic to discrete-time systems with a discontinuity in the form of their dynamics. In the time-dependent system, the validity of the dynamics remains limited to the area under the red parabola, and when the snapshot tori move and deform, some of their parts would end up outside the parabola if it was not for the aforementioned limitation. What happens instead is that these tendrils are abruptly cut off from the tori, which thus cease to remain closed curves and, therefore, break up. The cutoff parts then appear elsewhere in the phase space along the edge of the parabola, facing inwards with their vertex. Three of the larger cutoff tendrils can be observed in Fig. 3(c), as well as some still intact tori in the middle. Additionally, it is worth monitoring, along with the tori, the time evolution of chaotic seas as well. One observes that their instantaneous shape, the so-called snapshot chaotic seas, does not enter the cutoff tendrils of the snapshot tori (see Fig. S5 in the supplementary material).

Figure 4 illustrates the strong dependence of the final state on the scenario. The initial state is the same, $\alpha_0 = 70^\circ$ in all three cases, the difference between panels (a) and (b) is the final angle with the same number of steps, while the difference between panels (a) and

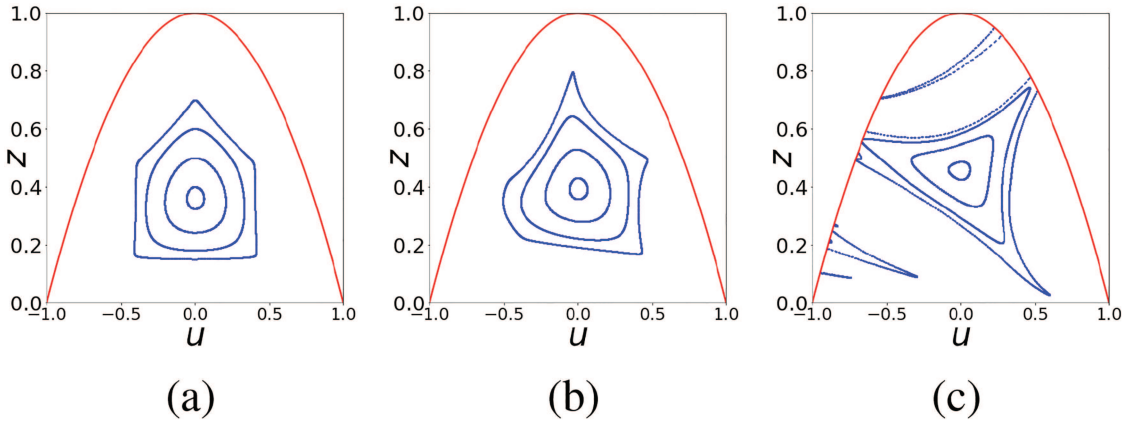

FIG. 3. Evolution of snapshot tori of the scenario $[70^\circ, 50^\circ, 10]$: (a) starting situation $n = 0$, (b) $n = 5$, and (c) $n = N = 10$. The initial conditions at $\alpha_0 = 70^\circ$ for the tori are $z_0 = 0.4, 0.5, 0.6, 0.7$, while $u_0 = 0$ for all. One can observe tori cut into several pieces in the last picture with some cutoff tendrils, which are, however, not yet strongly stretched.

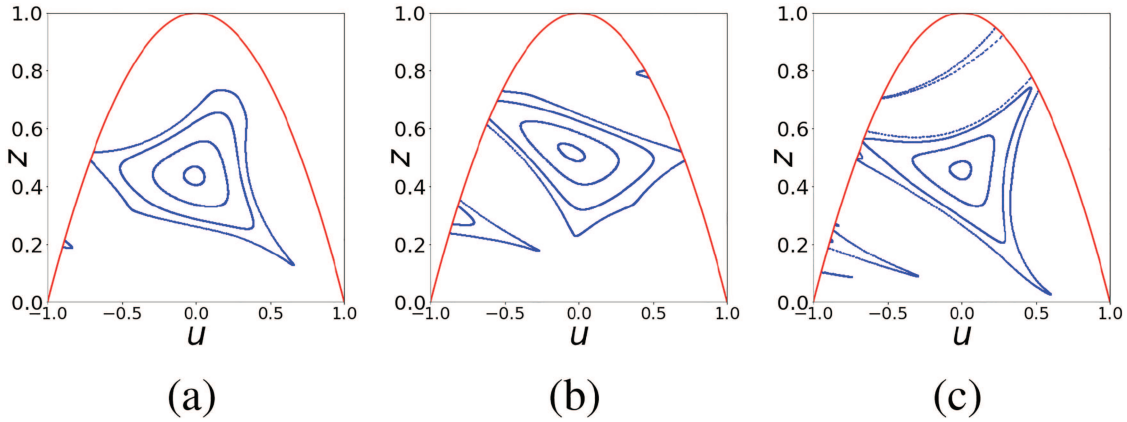

FIG. 4. The tori of Fig. 3 at the end of three different scenarios. (a) [70°, 50°, 5], (b) [70°, 40°, 5], and (c) [70°, 50°, 10]. The last picture is the same as Fig. 3(c), and one could notice that the scenarios of (b) and (c) are only different in one parameter from that of (a).

(c) is just in the number of steps. It is evident that a change in even one of the parameters of the scenario can lead to significant differences in the final outlook of the snapshot phase space, a property that can be better observed in this discrete-time system than in continuous ones.[1]

Another remarkable feature, the dramatic difference between the stationary phase space and that found with the parameter drift, is illustrated by the next picture (Fig. 5). Here, snapshot tori are shown to be present at angles where no macroscopic tori exist in the stationary case. Observe that in panel (b), the angle is $\alpha_{13} = 42°$, meaning that the scenario has now entered the region where, in the stationary case, the whole phase space is chaotic. It is, therefore, remarkable that up until this point, all of the snapshot tori have remained intact, closed curves. We can see the ending of this feature at $\alpha_{15} = 40°$ in (c), where the tori start to become cut into pieces. Note that the survival of tori under 45° is also exemplified in Fig. 4(b) but in a scenario in which only a single step (the last one) falls below that boundary.

B. The discontinuity condition

Figure 6 helps unfolding the condition for a snapshot torus becoming cut into pieces. Here, the evolution of a single torus is followed over a few steps along with the n-dependent line of discontinuity (7). In panel (a), the torus just comes close to the red bounding parabola but does not touch it, while it has no common points with the green discontinuity line either. One step later, in panel (b), the torus crosses the instantaneous line of discontinuity, meaning that its arcs above and below this line will be mapped according to different formulas; therefore, the next image of the torus appears as being cut into two pieces. As we go further into the scenario, more and more pieces of the torus will be cut off this

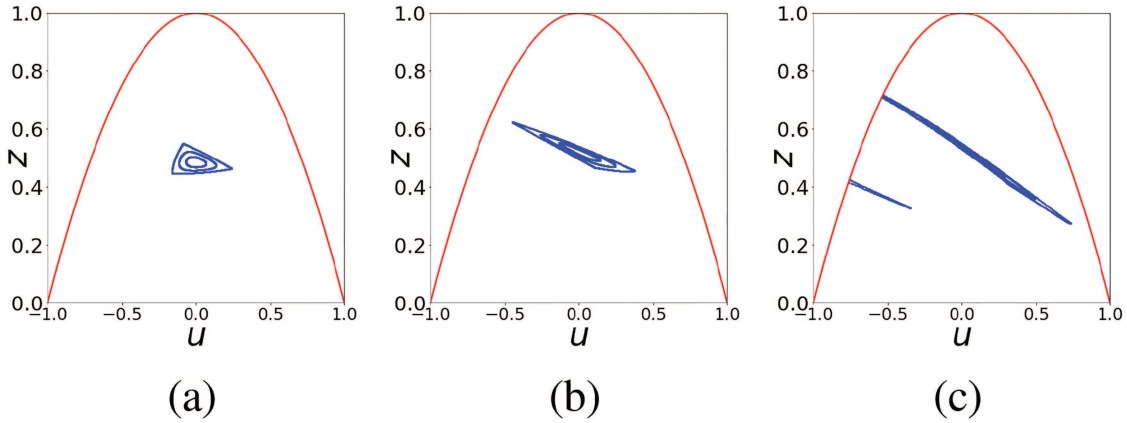

FIG. 5. Snapshot tori of the scenario [55°, 35°, 20], with initial conditions $z_0 = 0.375, 0.4, 0.475$ at $\alpha_0 = 55°$ and $u_0 = 0$ for all. The largest torus is close to the outermost KAM torus, separating the chaotic sea from the torus-dominated regime. Panels (a)–(c) display the steps $n = 9, 13, 15$ of the scenario.

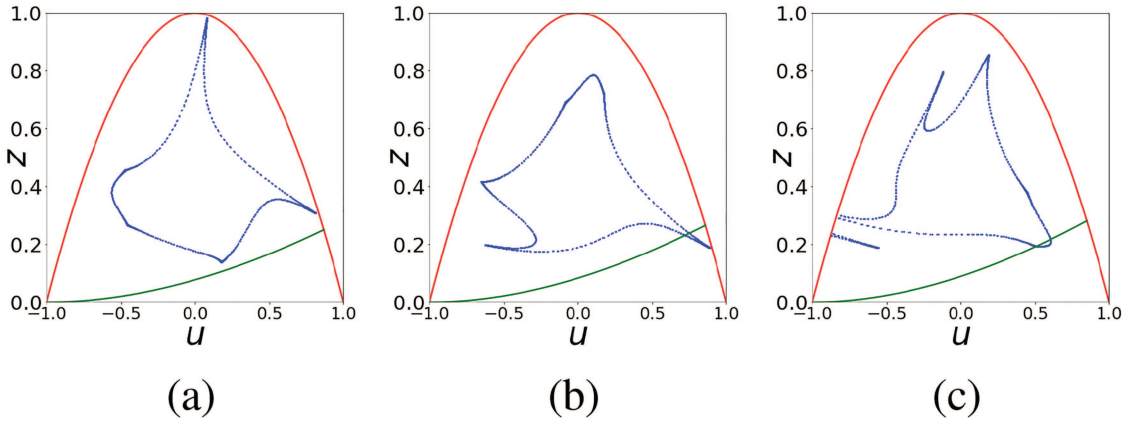

FIG. 6. Snapshot tori evolving from the initial condition $u_0 = 0$, $z_0 = 0.712\,28$ at $\alpha_0 = 70^\circ$ [approximately corresponding to the outermost KAM torus in Fig. 1(b)] displayed at steps $n = 10$ in (a), 11 in (b), and 12 in (c) of the scenario [70°, 50°, 20]. The green curve is the time-dependent boundary between the mappings (1) and (2), given by (7).

way. It is thus not the crossing of the parabola but rather the crossing of the discontinuity line that causes the breakup of the torus. Therefore, we call this mechanism as the *discontinuity condition* of torus breakup and denote its instant by n^*. Indeed, points on the line of discontinuity (7) are mapped on the entire parabola arc $z = 1 - u^2$ for any n, as follows from (7) and the non-autonomous form of (1) and (2).

IV. THE DYNAMICAL CONDITION

In Ref. 1, a general condition was formulated for the discrete time n_c from where a torus starts to be subjected to strong stretching. This was called the geometrical condition and differs from the discontinuity condition formulated in Sec. III, which is also geometrical in nature. For this reason, to highlight the distinction between the two, here, we call the condition defined in Ref. 1 the *dynamical condition*. While the discontinuity condition refers to the start of the torus being cut into different pieces, the latter is of different nature: it states that after the crossover time n_c, the torus starts to get strongly stretched and entrained into the chaotic sea in the form of thin arcs. This process and the two breakup conditions are visualized in Fig. S5 of the supplementary material. The instant n_c, as defined in Ref. 1, signals the moment when the initial torus intersects the stable manifold of a hyperbolic point belonging to that moment, which is obtained by iterating a short interval about it backward n_c times. Since one obtains finite-time manifolds this way, the shape of the manifold depends somewhat on the length dl of the short segment which the iteration starts with. We choose dl to be comparable with the size of the chaotic sea existing about the hyperbolic point. Ideally, the hyperbolic point should be such a point that keeps its hyperbolic character throughout a scenario, as an analog of hyperbolic fixed points of the frozen-in case. In Ref. 1, such points were identified and found to move in the phase space as time goes on and thus termed *snapshot hyperbolic points* (SHPs). An analytic approximation of one specific SHP was also possible there; however, that is rather the exception than the rule, and indeed, we will not be able to find analytic expressions for any of the SHPs in our system.

Here, we apply the dynamical condition to discrete-time systems. In the lack of an explicit formula for SHPs, we shall approximate them with hyperbolic points of the stationary system belonging to angles corresponding to time instant n_c. The images of the short segment of length dl represent a kind of manifold whose shape might change dramatically from instant to instant due to the parameter drift. We, therefore, call such manifolds *snapshot manifolds*.

We have to take into consideration that, contrary to our experience with continuous-time systems, the nature—i.e., if the point is elliptic or hyperbolic—of the (stationary) fixed points is not always constant through the range of the angle values of the scenario. To give an example, the period-one fixed point (4) is hyperbolic for $\alpha < 45^\circ$ where the whole phase space is chaotic, and elliptic for $\alpha \geq 45^\circ$ where tori can be observed around it, as can be seen in Figs. 1(b)–1(d). To successfully apply the dynamical condition, it is necessary to initiate the construction of the snapshot stable manifold in a region where the fixed point is hyperbolic and therein lies the importance of the knowledge of the nature of fixed points.

An example of the validity of the dynamical condition with the period-one fixed point is shown in Fig. 7 using the scenario [50°, 30°, 20]. Panel (a) displays at $\alpha_0 = 50^\circ$ the stable manifold (pink curve) of the fixed point belonging to $\alpha_8 = 42^\circ$ obtained by iterating a short segment [pink line in panel (b)] about this point backwards $n = 8$ times. The initial shape of the torus of interest [which is inside an elliptic island in this case, see Fig. 1(d)] is plotted in blue in panel (a), and one sees that these two curves have just intersected each other and the dynamical condition is thus fulfilled. Panel (b) illustrates that the condition corresponds indeed to a situation when the eighth image of the torus (blue curve) intersects the initial segment of the stable manifold. The torus has indeed approached a hyperbolic point (and the surrounding hyperbolic region), and from here on (for $n > 8$), it is subjected to strong stretching. We thus conclude that the time instant of the dynamical condition is $n_c = 8$.

The fact that the dynamical condition is similar to the one shown here in maps without any discontinuity is illustrated with the example of a non-autonomous standard map in Sec. S2 of the supplementary material; see Fig. S3.

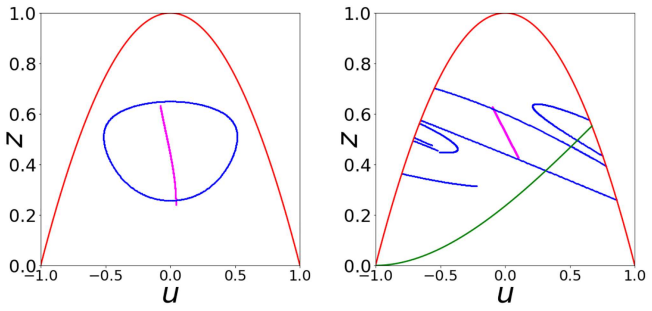

FIG. 7. (a) The snapshot stable manifold (pink curve) of the hyperbolic fixed point (4) of $\alpha_8 = 42°$, iterated backwards $n = 8$ times to $\alpha_0 = 50°$, where the displayed stationary torus (blue curve) of the initial condition $z_0 = 0.65$, $u_0 = 0$ lies. The two curves intersect, indicating that this will be the critical moment n_c according to the dynamical condition. (b) The result of scenario [50°, 30°, 20] at the $n = 8$th iterate, with the same torus seen stationary in (a). At this instance, the torus comes closer than the end points of the pink segment to the hyperbolic point fulfilling the dynamical condition. Also remarkable is that at $\alpha_0 = 50°$, the fixed point is elliptic, but the snapshot stable manifold exists, nevertheless, at this angle.

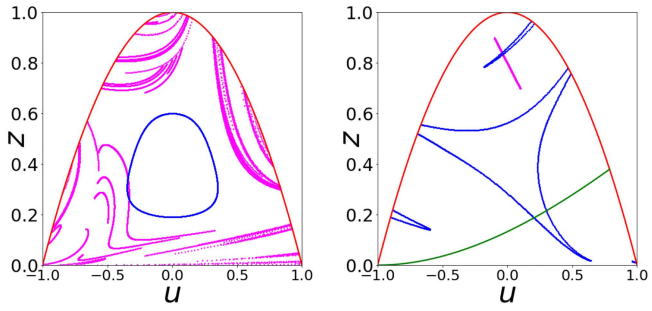

FIG. 8. (a) The snapshot stable manifold (pink) of the uppermost point of the three-cycle (5) of $\alpha_f = 52°$ iterated backwards $n = 15$ times, intersecting the stationary torus (blue) of the initial condition $z_0 = 0.6$, $u_0 = 0$ at $\alpha_0 = 67°$. It is remarkable that at this angle, the three-cycle does not even exist; however, its snapshot stable manifold does. (b) The same torus (blue) at the end of the scenario [67°, 52°, 15], intersecting the short pink segment around the uppermost cycle point, thus illustrating the validity of the dynamical condition: $n_c = 15$.

The example of Fig. 7 also draws attention to a rather counterintuitive phenomenon, namely, that stable manifolds exist at the initial state of the scenario (α_0), in spite of the fact that the (stationary) fixed point is *elliptic* there; it has changed its nature by reaching this angle. This indicates that the only thing that matters in this regard is that the fixed point is hyperbolic in the region from where the stable manifold is initiated irrespective of whether its nature changes during the scenario.

In Fig. 7(b), several cutoff pieces of the torus can be observed, which indicates that the breakup according to the discontinuity condition had already happened. In our system, the trend is that usually, the discontinuity condition is fulfilled first.

Since not all scenarios end under 45°, it is necessary to find other periodic cycles such that they are hyperbolic in the region $\alpha \geq 45°$ in order to apply the dynamical condition. The system's lacking another single fixed point necessitates that to this end, we look for higher order cycles. It would be convenient to first use a second-order cycle for our analysis. Its range of existence happens, however, to be $0 \leq \alpha \leq 45°$, meaning that it will not be of use for us.

Alternatively, we are going to work with a three-cycle the location of whose leftmost point is given by (5). An example for the dynamical condition provided by the uppermost point of this cycle can be seen in Fig. 8 in a scenario with $\alpha_0 = 67°$, $\alpha_f = 52°$, and $N = 15$. The nature of this cycle turns out to be the following. At 60°, the cycles start out elliptic, but this quickly changes at around 59.25°, from where it is hyperbolic before it reaches approximately 53.25°, when it again turns elliptic up until 44°, with a brief hyperbolic period between 52.5° and 51.5°. The scenario investigated in Fig. 8 ends at $\alpha_f = 52°$; therefore, this is indeed a suitable angle for the stable manifold to be initiated from since the cycle is hyperbolic here. Again, we see that the discontinuity condition was fulfilled first, and also that the stable manifold exists in Fig. 8(a). This is remarkable because the starting angle of the scenario is $\alpha_0 = 67°$, which is outside the range of existence of this cycle. Stable manifolds can thus survive not only in ranges where the fixed point is elliptic, but even in ranges where it *does not even exist*, reinforcing the idea that the only thing that matters here is that the fixed point is hyperbolic at the instant of n_c.

In Sec. VII, we show why a precise identification of a snapshot hyperbolic point is, in general, not needed for the formulation of the dynamical condition. What is needed instead is the stable foliation of the snapshot chaotic sea, which turns out to be an appropriate tool in any system and can also be approximated by the stable manifold emerging from properly chosen stationary cycle points.

V. DYNAMICAL INSTABILITY

The dynamical instability of stationary chaotic systems is typically characterized by the average growth rate of distances between pairs of points initially lying very close to each other.[40] In Ref. 1, it was shown that this can be generalized for a snapshot torus by considering the quantity $\rho(t) = \langle \ln r(t) \rangle$, which we will call *ensemble-averaged pairwise distance* (EAPD) with $r(t)$ being the distance of the point pairs at time t averaged over the ensemble (which is denoted by the brackets). It was also demonstrated that the dynamical instability of time-dependent Hamiltonian systems, when followed through the scenario of a snapshot torus, exhibits a pattern such that the distance initially hardly changes; however, the growth rate turns exponential when the snapshot torus breaks up. After this instance, the dynamics is chaotic and the Lyapunov exponent read off from the exponential range is unique in the sense that it characterizes the snapshot torus and the scenario and can only be measured some time after the start of the process.

A typical example of the double wedge system is shown in Fig. 9 with two scenarios ending under 45°. Now, the tori have two breakup conditions: the discontinuity (n^*) and dynamical (n_c) conditions. Both these instances are displayed in the figure, as well as

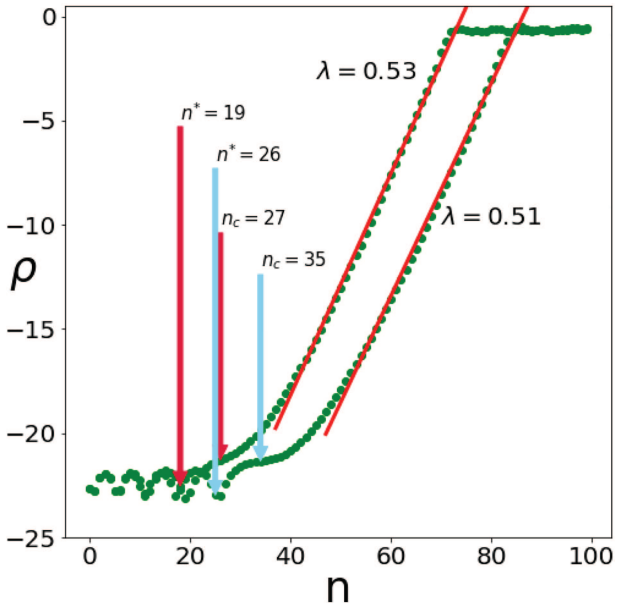

FIG. 9. Dynamical instability in the scenarios [50°, 30°, 100] and [50°, 35°, 100] for the initial torus generated from $u_0 = 0$, $z_0 = 0.65$ for both. The positions of both breakup conditions are marked with pink arrows for the upper and light blue arrows for the lower curve, with n_c visibly being close to the starting point of the exponential growth in both cases. As expected, the breakup occurs later in the second, slower scenario. The Lyapunov exponent λ characteristic of these processes are clearly observable as the slopes of the fitted red lines.

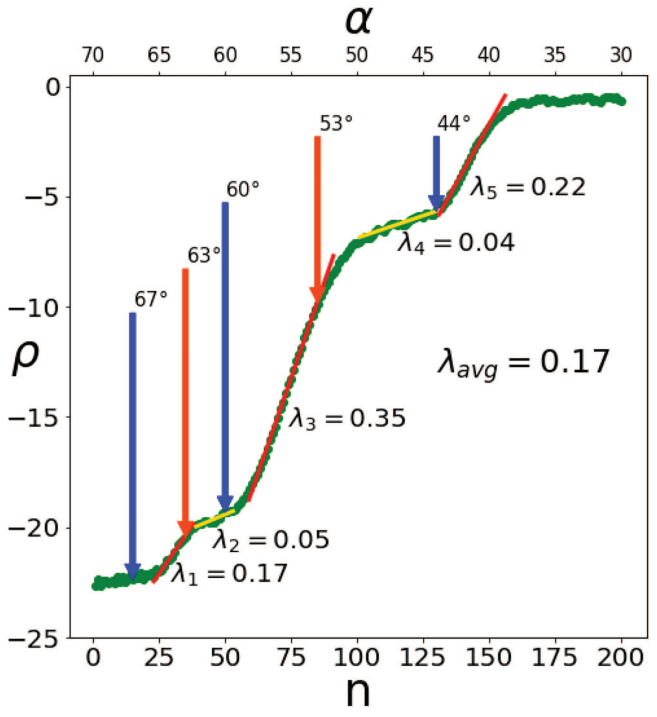

FIG. 10. Dynamical instability in the scenario [70°, 30°, 200] with the initial torus generated from $u_0 = 0$, $z_0 = 0.7$. The angles (rounded to a whole number in degrees) where the three- or four-cycles change their nature to hyperbolic (elliptic) are marked by blue (orange) arrows. Red (yellow) lines are fitted onto the steeper (flatter) parts and consequently correspond to larger (smaller) Lyapunov values. It is remarkable that blue arrows are generally followed by larger Lyapunov exponents, while orange ones are followed by smaller ones, revealing the nature of fixed points as a governor of the fine structure of the dynamical instability of snapshot tori.

the values of the Lyapunov exponents. As we can see, the trend that $n^* < n_c$ holds true here as well. One can also observe that it is n_c that appears to be the crossover time between a hardly changing phase and an exponential growth since it is situated at the beginning of the slopes. The reason for this is that while the discontinuity condition has parts of the torus cut off and thus making it break up, this not necessarily means that points of the torus are subjected to strong stretching [see Fig. 3(c), for example], which would lead to chaotic behavior.

The dynamical instability can be monitored for *any* torus of the initial phase space in the same scenario, as Fig. S4 in the supplementary material demonstrates for the standard map. The second curve in Fig. 9 illustrates that the crossover time n_c and the Lyapunov exponent of the exponential growth are different. In fact, all particular EAPD curves depend not only on the torus on which the ensemble is initiated but also on the scenario. For slower scenarios, n_c is expected to be larger and—in the spirit of the theory of adiabatic invariants[2–5]—is infinity for infinitesimally slow scenarios. The fact that the crossover times n_c found in our examples are on the order of tens of the iterate illustrates that the scenarios are relatively fast.

When investigating scenarios having a significant part within the $\alpha > 45°$ range, one finds that a clearly observable fine structure emerges, as Fig. 10 illustrates. The outlook of the fine structure turns out to be dependent on the nature of the cycles throughout the scenario. In demonstrating this in Fig. 10, we use two cycles: the three-cycle whose definition was described in Sec. II A and its nature in Sec. IV, and a four-cycle with three members above and one below the discontinuity line. The leftmost member is given by (5) with a different (and much more complicated) value of Γ^2. This four-cycle starts out hyperbolic from around 67°–63°, and then it turns elliptic until 59° after which it remains hyperbolic until its disappearance at about 56°. The most important points where the respective cycles turn hyperbolic are marked by blue arrows in Fig. 10, whereas orange ones indicate the starting points of the elliptic intervals. An important observation can be made based on the positions of the arrows; namely, that the parts where the cycles are elliptic are flatter (the Lyapunov value is smaller), while the hyperbolic parts are steeper (with larger Lyapunov values). Thus, the nature of stationary periodic cycles seems to leave its fingerprint on the fine structure of the dynamical instability with hyperbolicity accelerating and ellipticity slowing the process.

After the first (blue) arrow in Fig. 10, there is a small delay in the distance growth. The cause of this is that the snapshot torus actually has to come close to the hyperbolic point; i.e., the crossover time

n_c has to be reached, whose value in this scenario is 30, which is about where the first slope starts. When comparing Figs. 10 and 9, one finds that the average Lyapunov value (i.e., the one obtained by fitting to the whole exponential section) and even those of the steeper slopes found in the former are smaller than the ones in the latter. This is in line with the interpretation explained above: under 45°, the full stationary phase space is dominated by chaos and this results in a consistent, much stronger exponential distance growth.

VI. SCENARIOS WITH A NON-MONOTONOUS PARAMETER CHANGE

A. Scenarios with plateau ending

It is interesting to investigate scenarios in which a monotonous change in the angle, considered up to now, is augmented with another part. First, we choose the new part to be a plateau; i.e., the scenario ends with a fixed angle, which remains unchanged up to unlimited times. An interesting question is how the phase portrait characteristic of this stationary angle becomes visible in the fate of snapshot tori.

As a first example, we start with $\alpha_0 = 70°$ and a relatively large [but not the largest in Fig. 1(b)] torus. The final angle, i.e., the plateau value will be $\alpha_p = 55°$. Since the phase portrait belonging to it, shown in Fig. 1(c), will be solely responsible for the time evolution of the torus from here on, we superimpose a characteristic feature of it when plotting the instantaneous shape of the snapshot torus. This feature is the outermost KAM torus specified with some finite numerical accuracy (green curve in Fig. 11) of the $\alpha = 55°$ case. It, therefore, signals the boundary between tori and the chaotic sea on the plateau. Four characteristic instances are shown in Fig. 11. Panel (a) exhibits the snapshot torus at the instance of reaching the plateau: since an angle increment $\Delta\alpha = -0.5°$ is used, this is the 30th iteration. The snapshot torus is seen to be completely outside of the green curve, i.e., inside the chaotic sea of the stationary phase space of the plateau. The next panels show the points of the torus (in blue) 5, 15, and 50 iterates later. Since the whole torus is located inside the chaotic sea of the final state at $n = 30$, the dynamical condition can be considered fulfilled at this instance; $n_c = 30$. It is remarkable that the breakup process of the snapshot torus appears to take considerable time despite the fact that all of its points are inside the stationary chaotic sea of the plateau. Note that in Fig. 11(a), the torus is still intact; therefore, in this case, $n^* > n_c$ holds. After five more iterates [panel (b)], the torus just has a few pieces cut down (according to the discontinuity condition), and remnants of its structure are still observable after the 15th step on the plateau [panel (c)] as well. For a full mixing, a much longer time is needed; see panel (d). Since the snapshot torus turned out to be completely in the chaotic sea upon arriving at the plateau, after longer times, its points remain to avoid the elliptic island and spread out over the chaotic sea. The situation is somewhat similar to what we saw in a monotonic scenario ending below 45° (see Fig. 5) with the difference being that in that case, the phase space is uniformly chaotic at the end. The divided phase space of our example leads to a much more structured torus evolution than there.

The next example is similar, just the plateau is at $\alpha_p = 50°$, which possesses a much more divided phase space with four large elliptic islands [see Fig. 1(d)], and the initial torus is larger. In analogy with the previous case, here, we plot in green the approximate boundary of these four islands (three of which arise from a period-3 quasiperiodic motion). The angle difference is $\Delta\alpha = -1°$, and the plateau value is arrived at after 20 steps. As panel (a) of Fig. 12 shows, the snapshot torus possesses points in all the islands and a few outside of them, too, at this instant. The fact that part of the snapshot torus is located inside the large elliptic islands means that its points will not be mixed even after longer times, as proven by the other panels. In fact, even after 50 iterations on the plateau, long segments of the snapshot torus appear as continuous curves.

These different time evolutions of snapshot tori lead to differences in the strength of dynamical instability on the ρ vs n curves; see Fig. 13. In the first case (upper curve), we see that the exponential increase starts immediately after arriving at the plateau. As another feature, the saturation of ρ occurs not around zero, rather at a slightly negative value, indicating that a full stretching across the phase space is hindered by a small island in the middle [see Fig. 1(c)]. The lower curve belongs to the scenario of Fig. 12. The striking difference is that after an increase of ρ has started, the slope

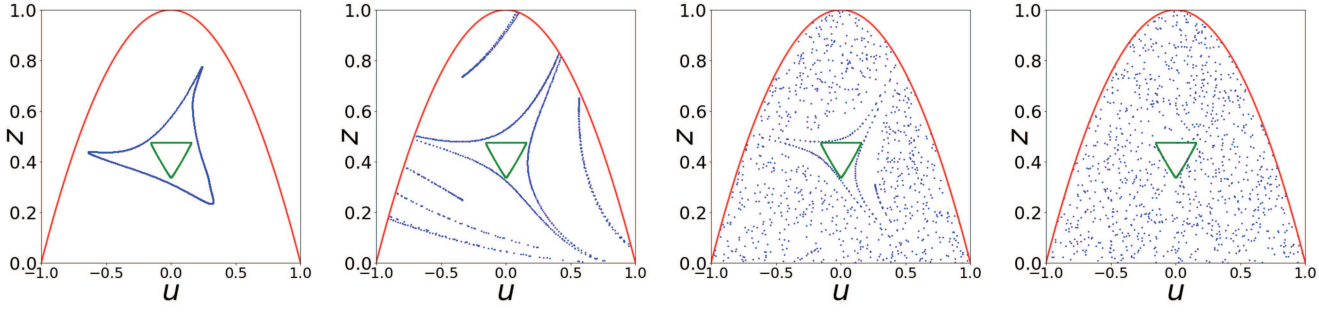

FIG. 11. Scenario with a plateau at $\alpha_p = 55°$. The preceding scenario is [70°, 55°, 30] with the initial condition $u_0 = 0$, $z_0 = 0.55$. The images of the blue torus are taken at different times on the plateau; these are in order of labels (a) to (d): $n' = 0, 5, 15, 50$. The green curve of the initial condition $u_0 = 0$, $z_0 = 0.475$, is practically the outermost torus on the stationary phase space of the plateau [see Fig. 1(c)].

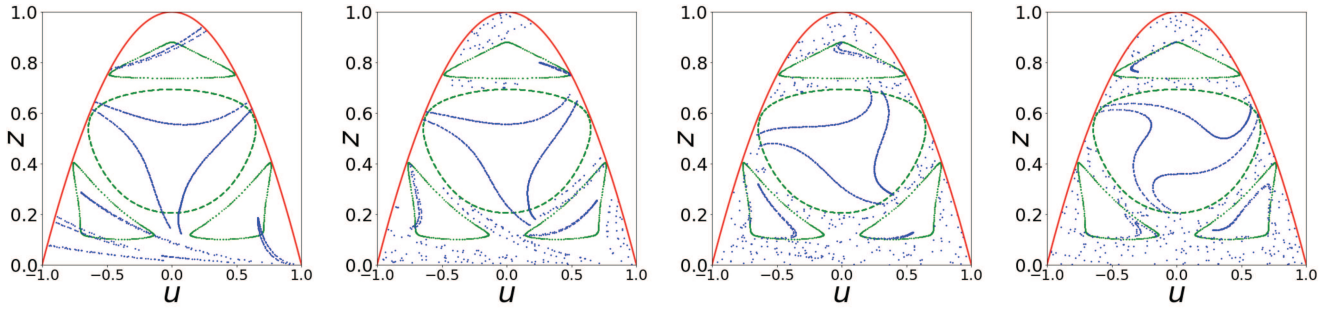

FIG. 12. Scenario with a plateau at $\alpha_p = 50^\circ$, with the preceding scenario of $[70^\circ, 50^\circ, 20]$ and the initial condition $u_0 = 0$, $z_0 = 0.6$. The images (a)–(d) are taken at $n' = 0, 5, 15$, and 50 steps on the plateau, respectively. The initial conditions of the green boundary tori are $z_0 = 0.695, 0.88$ and $u_0 = 0$ [see Fig. 1(d)].

is much lower and the λ value is significantly smaller. The reason is that when evaluating ρ, the distance between all point pairs of the original torus is considered, and because there are large islands at the end state, containing points of the torus, pairs without an exponential divergence are also included in the average. When more torus points fall into the chaotic sea when arriving at the plateau, the patterns are different and the Lyapunov exponent can be larger as Figs. S6 and S7 in the supplementary material illustrate.

A simple quantitative argument can be used to understand the main features of the EAPD ρ_n *after reaching the plateau*. This is based on the fact that points of the original torus are, upon arriving on the plateau, either in the chaotic sea or in the quasiperiodic islands of a stationary problem. We simply assume that the distance of all pairs with at least one element in the chaotic sea follows the rule

$$r^c_{n'} = \begin{cases} r_0 e^{\lambda n'} & \text{if } n' \ll n'_S, \\ r_{max} & \text{if } n' \gg n'_S, \end{cases} \tag{8}$$

where r_0 is the distance of the point pairs when arriving at the plateau, λ is the Lyapunov exponent of the chaotic sea in the stationary problem of the plateau, n' is the number of iterations spent on the plateau, n'_S is a saturation value after which pairs are stretched practically across the whole phase space, and r_{max} (a quantity of order unity) is their typical distance. Concerning pairs in the elliptic islands, we simply assume that their distance practically does not change: $r^e_{n'} \approx r_0$. Since ρ_n is the average of all logarithmic distances $\ln r_n$ of pairs, in this simplified picture, it has two terms only: $\rho_{n'} = p \ln r^c_{n'} + (1-p) \ln r^e_{n'} = p \ln (r^c_{n'}/r_0) + \ln r_0$, where p represents the proportion of point pairs of the original torus with at least one element in the chaotic sea at $n' = 0$. Substituting (8), we obtain

$$\rho_{n'} = \begin{cases} p\lambda n' + \ln r_0 & \text{if } n' \ll n'_S, \\ p \ln r_{max} + (1-p) \ln r_0 & \text{if } n' \gg n'_S. \end{cases} \tag{9}$$

This indicates that the value of the slope on the plateau is $p\lambda$. This is close to the Lyapunov exponent of the stationary case only if practically the entire torus has arrived at the chaotic sea of the plateau. In such a case, function ρ_n levels off close to unity as the upper graph of Fig. 13 exemplifies. In other cases, e.g., the lower curve, the leveling off occurs at a much smaller value, reached along a much weaker slope, both being proportional to p.

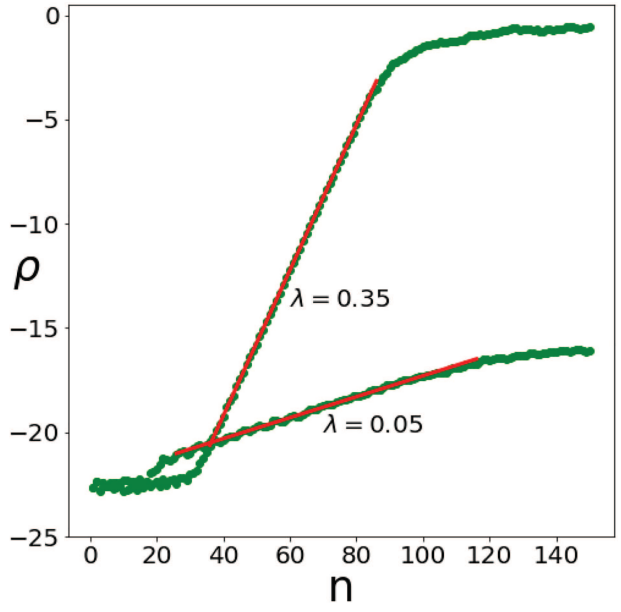

FIG. 13. Dynamical instability of the plateau scenarios of Figs. 11 (upper curve) and 12 (lower curve). As we can see, the Lyapunov exponent is much smaller on the latter, which is due to parts of its snapshot torus being trapped in the elliptic islands of the stationary phase space of the plateau.

B. Scenarios with full return

Another interesting case to be investigated is the so-called return-scenario, where after a monotonous parameter change with $\Delta\alpha$, we apply the same scenario again, but this time using $-\Delta\alpha$, and thus arriving back at the starting angle. Figure 14 shows a typical example of return-scenarios, applied to the entire phase space—including the chaotic sea—of $\alpha_0 = 70^\circ$ shown in panel (a). The midpoint at 50°, reached in 20 steps ($\Delta\alpha$ is negative), can be

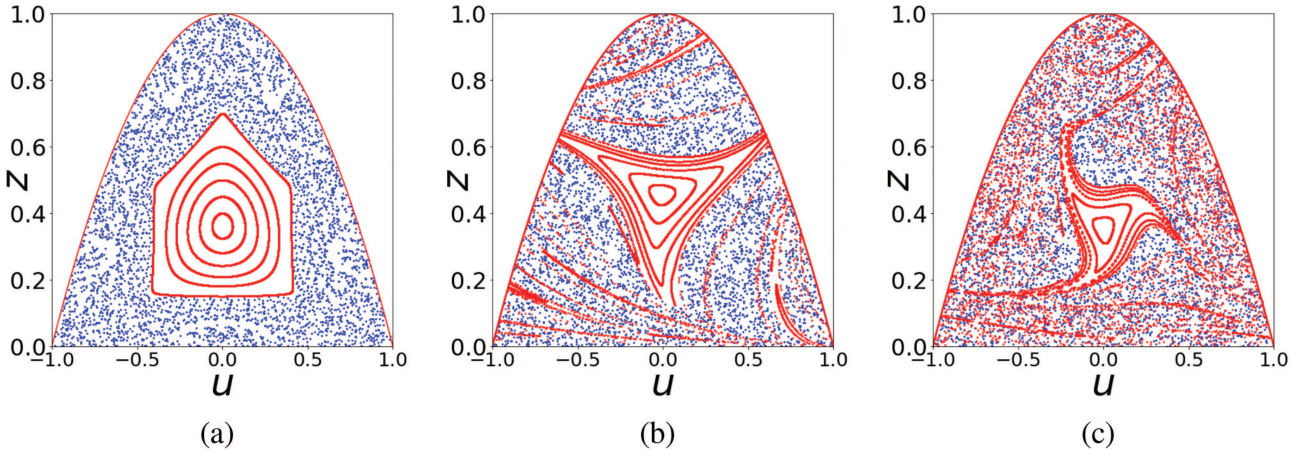

FIG. 14. Hysteresis in a return-scenario. (a) The starting state of 70° is similar to that of Fig. 1(b). The initial conditions were chosen so that the tori (red) are about the same distance from each other and to provide a clear representation of the chaotic sea (blue dots) as well. (b) End state of the scenario [70°, 50°, 20]. From here on, scenario [50°, 70°, 20] is applied, and the end state can be seen in panel (c). It very much differs from the starting state, meaning that a hysteresis has taken place.

seen in panel (b), where several tori have already broken up according to the dynamical and discontinuity conditions. Up to this point, the scenario is just a typical monotonous parameter change considered in Secs. II–V. From here on, however, we switch the direction of the parameter change while leaving all other aspects of the scenario the same, meaning that the angle will now increase back to 70° after the same number of steps ($\Delta\alpha$ is positive). The end of this process can be seen in panel (c). This, despite being at the same angle as the starting state, very clearly differs from the phase space in panel (a), meaning that the return-scenario results in a hysteresis of the phase space. Out of the initial six tori, at the midpoint of the scenario—as expected—a number (namely, 3) have already broken up; however, it is remarkable that out of the remaining three, two have remained closed curves until the end of the whole return-scenario as well. The others are strengthening the chaotic sea, which in turn increases in size. The presence of a hysteresis is a clear indication of the scenario *not being adiabatic*.

VII. STABLE AND UNSTABLE FOLIATIONS OF THE SNAPSHOT CHAOTIC SEA

Chaotic seas become snapshot chaotic seas when the system is subjected to parameter drifts, while their shape is changing and their extension is typically increasing as snapshot tori become broken up and mixed into them. It is, therefore, useful to explore the stable and unstable foliations of these novel type of chaotic seas, which shed new light on the dynamical condition too, as we shall soon demonstrate.

Traditional (stationary) chaotic seas are *densely* foliated by these two types of foliations,[40] which is approximated by the stable and unstable manifolds of any hyperbolic cycle embedded into the sea. The manifold of any given hyperbolic cycle is expected to run approximately very close and practically parallel to those of the others. Because of this, in spite of the fact that the chaotic sea is the closure of all these manifolds, an appropriate visual impression can be obtained by observing the manifolds of a single cycle point.

In cases with the parameter drift, if known, SHPs within the chaotic sea can be used for the exploration of the foliations. With the lacking of the knowledge of their precise location, a more qualitative way can also be followed (which also holds in traditional cases): consider a finite line segment running approximately parallel to the anticipated direction of the stable (unstable) foliation and iterate it backward (forward). The segment will be stretched and folded, and after a sufficiently large number of iterations, it approximates the foliation requested. An unprecise choice of the initial direction only makes the convergence somewhat slower since the segment needs to be turned into the appropriate direction during the first few steps, but this is a minor effect as the convergence is expected to be exponentially fast in the middle of the sea at least, where the dynamics is uniformly hyperbolic.

Consider first the chaotic sea of a stationary case and mark in it the points of a long chaotic trajectory. Locate a few line segments in the middle of the sea. Iterate the segments backward (forward) according to a scenario, along with the points of the chaotic sea. The images of these points represent the backbone of the snapshot chaotic sea in states reached during the scenario (blue dots in Fig. 15). The segments become stretched and folded and shade (pink curves), after some time, the area defined by the blue points, which can also be seen in Fig. 15. The shading is the consequence of the fact that the original chaotic sea is dense, and this property remains true when a scenario is applied: close to any blue points, there are points of the foliations. One property changes; however, points of originally quasiperiodic islands become entrained into the sea in the form of white bands that increase in number and decrease in widths.

The fact that the originally quasiperiodic regions become mixed with the chaotic sea as time goes on shows that snapshot chaotic seas are *not* dense. This leads to a remarkable property: when making the same numerical experiment as above, just starting from

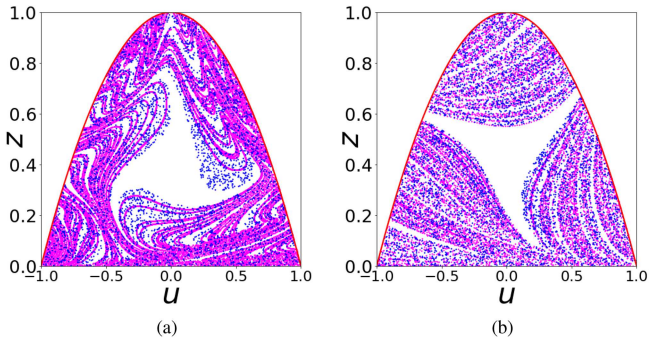

FIG. 15. Snapshot stable (a) and unstable (b) foliations (pink lines) plotted along with snapshot chaotic seas (evolved from stationary ones) arising by the end of the scenarios [53°, 63°, 20] (a) and [67°, 52°, 30] (b) (blue dots). (These differ in their initial states and lengths for visualization purposes only.) The foliations were started from three vertical segments of length $dl = 0.2$ chosen in different parts of the initial chaotic sea. The pink line has not yet fully shaded the blue-dotted regions since the number of iterations is only 20 and 30 in these examples. White bands can be seen entrained into the area covered by the snapshot chaotic seas, signaling the breakup of tori.

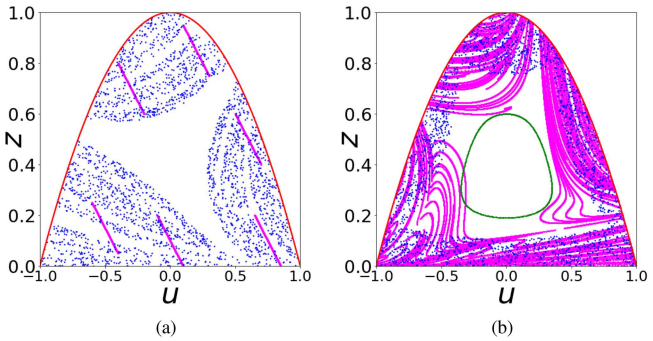

FIG. 17. The generalized dynamical condition for the same torus and scenario as that of Fig. 8, using the stable pseudo-foliation. (a) The snapshot chaotic sea (blue dots) at the end of the scenario [67°, 52°, 15] evolved from the initial chaotic sea at 67°, as generated from $z_0 = 0.1, 0.9$, $u_0 = 0$. A stable pseudo-foliation is initiated within this snapshot chaotic sea from the pink segments, the location of whose was chosen to represent all major parts of the snapshot chaotic sea while not having any portions outside it. (b) The stable pseudo-foliation of the snapshot chaotic sea at instant zero, obtained by iterating the pink segments backwards 15 times, plotted together with the investigated stationary torus (green) and the chaotic sea itself (which has returned to its initial state).

a snapshot chaotic sea (instead of a stationary one), one finds that, after some time, the approximate stable foliation *extends outside the snapshot chaotic sea of that instant*: it develops tendrils, which leave the blue-dotted region. This is a consequence of the fact that the initial segment crosses through both the snapshot chaotic sea and the entrained white bands. Those parts of the segment that are originally within the sea remain within, but the others stretch outside the sea. We call, therefore, the foliation generated this way the stable *pseudo-foliation*. An example for this is shown in Fig. 16(a). In contrast, the unstable pseudo-foliation of a snapshot chaotic sea, however, does not leave its area, as can be seen in Fig. 16(b). To generate the unstable manifold, one has to do forward iteration, a process during which the snapshot chaotic sea grows (entraines tori) and thus does not let the unstable foliation leave its area. The reason for the broken symmetry between the structure of stable and unstable pseudo-foliations will be explored in a future paper.

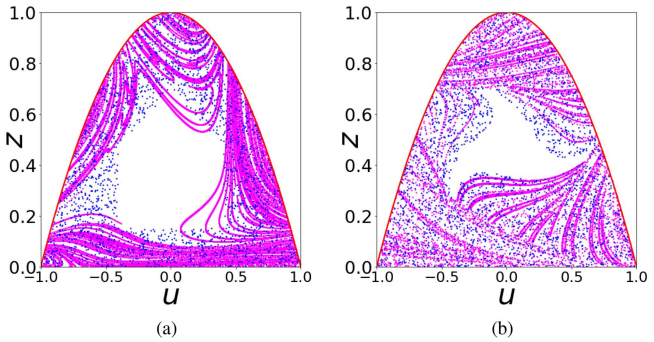

FIG. 16. (a) Stable pseudo-foliation of a snapshot chaotic sea arising by the end of the scenario [70°, 50°, 20]. This chaotic sea was then iterated back to its starting state in 20 steps (blue dots), while simultaneously, the stable pseudo-foliation (pink lines) was constructed by iterating three vertical segments of length $dl = 0.2$ by the same number of steps. Note that the pseudo-foliation leaves the snapshot chaotic sea (blue-dotted region). (b) Unstable pseudo-foliation (pink lines) of a snapshot chaotic sea. The snapshot chaotic sea arising by the end of the scenario [70°, 65°, 10] was iterated over 30 additional steps with the same $\Delta\alpha = -0.5°$ as in the scenario, along with three vertical segments. This pseudo-foliation does not leave the snapshot chaotic sea (blue-dotted region).

This observation has an important consequence for the dynamical condition of torus breakup discussed in Sec. IV. It is not necessary to consider the stable manifold of a specific SHP (or an approximant of it) and if it crosses the original torus, as any other SHP would do. In fact, more generally speaking, it is best to consider the whole stable pseudo-foliation of the snapshot chaotic sea. Thus, a generalized formulation of the dynamical condition is that a torus breaks up after n_c iterates, in the sense that it will be subjected to strong stretching from that time on when *the stable pseudo-foliation of the snapshot chaotic sea belonging to time instant n_c first intersects the initial torus*. The advantage of defining the dynamical condition this way is that while providing a good approximation for the value of n_c, it does not require any knowledge of the SHPs whatsoever. Thus, this is a good formulation of the dynamical condition in *any* Hamiltonian system with parameter drifts even those where no analytic expressions for the SHPs exist, like the one studied here. Figure 17 shows an example of this on the same scenario as that of Fig. 8. We see that the foliation intersects the torus (for the first time), meaning that $n_c = 15$. Thus, for this scenario, the generalized dynamical condition provides the same result as the original one. This is, however, not always the case: the two versions of the dynamical condition might lead to slightly different n_cs since the construction starts from a segment of finite length dl, and only a finite number of iterations are carried out. There is thus some variance in the possible outcomes for n_c.

VIII. SUMMARY

When conservative systems described by mappings are subjected to parameter drifts, snapshot tori originating from the stationary system deform as time goes on, allowing for a similar treatment of these systems to time-continuous ones described in Ref. 1. In special cases, physical reasons might lead to a discontinuity in the dynamics, leading to the cutting of the tori into pieces as they hit the line of discontinuity, called the discontinuity condition. While presenting this phenomenon as well, the following findings of this study are applicable to any discrete system irrespective of the presence of discontinuity in them. A critical event in the evolution of the torus (or pieces of it) is when they enter a region of intense stretching. From here on, the points originating from a stationary torus become mixed into the snapshot chaotic sea. The dynamical condition for the start of intense stretching translates to a crossover time n_c after which the ensemble starts exhibiting chaos-like dynamics. Geometrically, this can be formulated as the intersection of the original torus with the stable manifold of a snapshot hyperbolic point (SHP). Since the precise locations of SHPs are not known in general, approximate points can also be used, but the investigation of the foliations of snapshot chaotic seas provides the way for a more general formulation. Specifically, it is the stable foliation of the snapshot chaotic sea obtained by iterating a finite initial segment backwards, termed the stable pseudo-foliation, which can be used as a tool. This foliation extends beyond the instantaneous chaotic sea, and the intersection of it with the initial torus provides the generalized dynamical condition. After the dynamical condition is fulfilled, the stretching is so strong that the ensemble emanated from the original torus exhibits exponential stretching on average, which can be monitored by the so-called ensemble-averaged pairwise distance (EAPD), denoted by $\rho(t)$, the slope of which can be considered an instantaneous Lyapunov exponent. The strongly non-monotonous parameter dependence of the phase space in the stationary mapping might lead to the alteration of stronger and weaker dynamical instability (larger and smaller instantaneous Lyapunov exponents) along a monotonous parameter drift scenario. The dynamics of systems with more general parameter drifts is rather complex and not yet fully explored; however, one could expect that the main properties found here, such as the breakup of tori and the deformation of the chaotic sea, would remain the key features in those systems as well, illustrated by the examples of scenarios ending on plateaus or with full return.

SUPPLEMENTARY MATERIAL

See the supplementary material for the derivation of a more general, although dynamically similar mapping, the case of the standard map as an additional example for conservative maps subjected to parameter drifts, and additional figures on the temporal evolution of chaotic seas as well as on plateau ending scenarios.

ACKNOWLEDGMENTS

We would like to thank G. Györgyi and G. Károlyi for beneficial discussions and comments. Special thanks to T. Kovács for a comment directing our attention to the unusual features of snapshot chaotic seas. This work was supported by the Hungarian NKFIH Office under Grant No. K-125171.

DATA AVAILABILITY

The data that support the findings of this study are available from the corresponding author upon reasonable request.

REFERENCES

[1] D. Jánosi and T. Tél, Chaos **29**, 121105 (2019).
[2] E. Ott, Phys. Rev. Lett. **42**, 1628 (1979).
[3] R. Brown, E. Ott, and C. Grebogi, Phys. Rev. Lett. **59**, 1173 (1987).
[4] R. Brown, E. Ott, and C. Grebogi, J. Stat. Phys. **49**, 511 (1987).
[5] M. Wilkinson, J. Phys. A **21**, 4021 (1988).
[6] G. Haller, Annu. Rev. Fluid Mech. **47**, 137 (2015).
[7] G. Haller and F. J. Beron-Vera, J. Fluid Mech. **731**, R4 (2013).
[8] G. Haller, A. Hadjighasem, M. Farazmand, and F. Huhn, J. Fluid Mech. **795**, 136 (2016).
[9] G. Froyland and O. Junge, SIAM J. Appl. Dyn. Syst. **17**, 1891 (2018).
[10] A. G. Ramos *et al.*, Sci. Rep. **8**, 4575 (2018).
[11] J. S. E. Portela, I. L. Caldas, R. L. Viana, and M. A. F. Sanjuán, Int. J. Bifurcat. Chaos **17**, 4067 (2007).
[12] J. S. E. Portela, I. L. Caldas, and R. L. Viana, Eur. Phys. J. Spec. Top. **165**, 195 (2008).
[13] A. C. Fraile, Jr., M. Roberto, I. L. Caldas, and C. G. L. Martins, IEEE Trans. Plasma Sci. **45**, 2906 (2017).
[14] D. de O. Berto, L. F. Ziebell, and P. R. da S. Rosa, Plasma Phys. Control. Fusion **61**, 065021 (2019).
[15] R. Bürkle, A. Vardi, D. Cohen, and J. R. Anglin, Phys. Rev. A **99**, 063617 (2019).
[16] R. Bürkle, A. Vardi, D. Cohen, and J. R. Anglin, Phys. Rev. Lett. **123**, 114101 (2019).
[17] F. G. Montoya, F. Borondo, and C. Jung, Commun. Nonlinear Sci. Numer. Simul. **90**, 105282 (2020).
[18] F. Revuetta *et al.*, J. Chem. Phys. **147**, 074104 (2017).
[19] M. Fedmaier *et al.*, J. Phys. Chem. B **123**, 2070 (2019).
[20] F. J. Romeiras, C. Grebogi, and E. Ott, Phys. Rev. A **41**, 784 (1990).
[21] L. Yu, E. Ott, and Q. Chen, Phys. Rev. Lett. **65**, 2935 (1990).
[22] Y.-C. Lai, U. Feudel, and C. Grebogi, Phys. Rev. E **54**, 6070 (1996).
[23] Y.-C. Lai, Phys. Rev. E **60**, 1558 (1999).
[24] R. Serquina, Y.-C. Lai, and Q. Chen, Phys. Rev. E **77**, 026208 (2008).
[25] M. Ghil, M. D. Chekroun, and E. Simonnet, Physica D **237**, 2111 (2008).
[26] C. Kuehn, *Multiple Time Scale Dynamics* (Springer, New York, 2015).
[27] M. Ghil, *Climate Change: Multidecadal and Beyond* (World Scientific, Singapore, 2015), Chap. 2, pp. 31–51.
[28] G. Drótos, T. Bódai, and T. Tél, J. Clim. **28**, 3275 (2015).
[29] B. Kaszás, U. Feudel, and T. Tél, Phys. Rev. E **94**, 062221 (2016).
[30] T. Haszpra and M. Herein, Sci. Rep. **9**, 3896 (2019).
[31] B. Kaszás, T. Haszpra, and M. Herein, Chaos **29**, 113102 (2019).
[32] T. Bódai, G. Drótos, M. Herein, F. Lunkeit, and V. Lucarini, J. Clim. **33**, 2163 (2020).
[33] S. Pierini, J. Stat. Phys. **179**, 1475 (2020).
[34] M. Vincze, I. Dan Borcia, and U. Harlander, Sci. Rep. **7**, 254 (2017).
[35] T. Kovács, J. R. Soc. Interface **17**, 20200648 (2020).
[36] Y.-C. Lai and T. Tél, *Transient Chaos* (Springer, New York, 2011).
[37] H. E. Lehtihet and B. N. Miller, Physica D **21**, 93 (1986).
[38] H. J. Korsch and H.-J. Jodl, *Chaos: A Program Collection for the PC*, 2nd ed. (Springer, Berlin, 1999).
[39] T. Tél and M. Gruiz, *Chaotic Dynamics* (Cambridge University Press, 2006).
[40] E. Ott, *Chaos in Dynamical Systems* (Cambridge University Press, Cambridge, 1993).